J Mater Sci (2025) 60:8749–8765

Computation & theory

Predictive study of Mn- and Co-based van der Waals compounds for spintronic and quantum applications

Al-Suwaychit Fadhil Noori Yaqoob[1], Zahra Nourbakhsh[1,*], and Daryoosh Vashaee[2,3,*]

[1] Faculty of Physics, University of Isfahan, Isfahan, Iran
[2] Department of Electrical and Computer Engineering, North Carolina State University, Raleigh, USA
[3] Department of Materials Science and Engineering, North Carolina State University, Raleigh, USA

Received: 24 January 2025
Accepted: 30 April 2025
Published online: 26 May 2025

ABSTRACT

This study investigates the structural, electronic, and magnetic properties of XBr_2, XI_2, and XBrI (X = Mn, Co) compounds using density functional theory, incorporating spin–orbit coupling and the GGA + U framework. Cohesive and formation energy calculations reveal that $MnBr_2$ is most stable in the ferromagnetic phase, while the other compounds favor antiferromagnetic ordering. The inclusion of the effective Coulomb screening potential (U_{eff}) enhances the localization of 3d orbitals, leading to increased magnetic moments. Electronic structure analyses show that most compounds transition to semiconducting behavior in the antiferromagnetic phase—except CoI_2—while $MnBr_2$, $CoBr_2$, and CoI_2 exhibit half-metallicity in the ferrimagnetic phase. In the antiferromagnetic phase, $MnBr_2$, MnI_2, and MnBrI display topological Dirac-like points between the *R* and Γ points, suggesting the presence of massless fermions and enabling phenomena such as the quantum Hall effect and ultra-high carrier mobility. The computational results are consistent with available experimental data, highlighting the potential of Mn- and Co-based van der Waals compounds for spintronic and quantum applications.

Introduction

The exploration of magnetic materials at reduced dimensionality has recently gained significant momentum due to their potential in advancing quantum and spintronic technologies. Two-dimensional (2D) magnetic materials, especially those with van der Waals (vdW) layered structures, enable fundamental studies of magnetism in low dimensions and offer new opportunities for ultra-compact, low-power device applications. One particularly attractive direction involves the use of such materials in spintronics, where both the charge and spin degrees of freedom of electrons are utilized to enhance memory density, logic performance, and energy efficiency. The concept of spin qubits in 2D materials further opens possibilities for quantum computing, where control over magnetic ordering and spin coherence is critical.

In this context, transition metal halides with the general formula MX_2 (M = transition metal; X = halogen) have emerged as promising candidates. Their magnetic ordering, electronic structure tunability, and

Handling Editor: Kevin Jones.

Address correspondence to E-mail: z.nourbakhsh@sci.ui.ac.ir; dvashae@ncsu.edu

https://doi.org/10.1007/s10853-025-10972-w

compatibility with 2D architectures make them ideal systems for realizing functionalities such as spin filtering, nonvolatile memory, magnetoelectric switching, and topological quantum phases. While recent studies have highlighted 4d and 5d transition metal-based MX_2 compounds due to their strong spin–orbit coupling (SOC), the 3d transition metal-based systems—such as MnX_2 and CoX_2—offer distinct advantages. These include more localized d electrons, rich magnetic phase behavior, and the possibility to capture strong electronic correlations using approaches such as DFT + U. Moreover, their elemental composition and synthesis routes are typically simpler and more scalable for experimental realization.

Several Mn- and Co-based MX_2 materials are known to exhibit half-metallic ferromagnetism, which is particularly valuable for spintronic applications. Additionally, these systems may display a range of magnetic states—ferromagnetic (FM), antiferromagnetic (AFM), or ferrimagnetic—along with topological features such as Dirac-like crossings near the Fermi level. These features support spin-polarized transport and could enable phenomena such as quantum anomalous Hall effects and spin Hall effects, providing platforms for low-dissipation electronics and quantum information devices.

MX_2 compounds, such as $MnBr_2$, MnI_2, $CoBr_2$, and CoI_2, possess a CdI_2-type hexagonal layered crystal structure with the space group $P\bar{3}m$ [1–4]. Their structural simplicity and magnetic diversity make them ideal candidates for first-principles investigations. Experimental studies have reported intriguing magnetic behavior in these systems. For instance, MnI_2 undergoes three successive magnetic phase transitions at low temperatures (3.95 K, 3.8 K, and 3.45 K), ultimately entering an antiferromagnetic state below 3.45 K [5]. Kurumaji et al. demonstrated that MnI_2 exhibits multiferroic behavior, with ferroelectric polarization induced by a helical spin structure aligned along the [110] direction [6]. This behavior was supported by the identification of a spiral spin crystal structure by Wu et al. [7] and magnetization studies by Li et al. that confirmed antiferromagnetic transitions near 4 K [1].

Optical and magneto-optical properties of MnI_2 have also been well documented. Hoekstra et al. reported absorption and magnetic circular dichroism spectra between 1.5 and 300 K, associating the features with d-d transitions of Mn ions [3], while additional optical measurements were conducted by Erk et al. [8]. CoI_2, another compound with a CdI_2-type structure and space group $P\bar{3}m$, remains stable up to its melting point (515 °C) [9]. Magnetic measurements have determined a Co-site magnetic moment of approximately 1.67 μB [10], and neutron diffraction and magnetization studies have confirmed its antiferromagnetic ground state, with spins aligned in-plane and coupled antiferromagnetically between layers due to easy-layer anisotropy [10–12]. Under external pressure (~ 10 GPa), CoI_2 exhibits an insulator-to-metal transition [12, 13].

The magnetic behavior of CoI_2 was further analyzed by Mekata et al., who identified a first-order magnetic transition at 9.4 K using neutron diffraction [14]. Theoretically, $CoBr_2$ has been proposed to host a topologically nontrivial magnetic state characterized by a Chern number of $Z = 4Z = 4Z = 4$ [15]. It also adopts a CdI_2-like structure with a small band gap (~ 0.2 eV) and lattice constants of $a = b = 3.738$ Å, $c = 16.907$ Å [16], and reported on-site Coulomb and exchange parameters of U = 1.3 eV and J = 0.3 eV, respectively. Below 19 K, $CoBr_2$ enters an antiferromagnetic phase with spins aligned perpendicular to the c-axis, as predicted by molecular field theory [17].

$MnBr_2$ is also of considerable interest. It crystallizes in a CdI_2 structure and displays antiferromagnetic ordering below 2.3 K, with spin moments perpendicular to the c-axis [18, 19]. Structural details include Mn^{2+} ions located at (0, 0, 0), with Br^- ions occupying (1/2,2/3,1/4) and (1/2,1/3,3/4) positions. Its lattice constants are $a = 3.868$ Å and $c = 6.272$ Å [20]. Like MnI_2, $MnBr_2$ remains stable in the AFM phase, with a reported Néel temperature around 2.16 K [21, 22].

Despite this extensive body of work, several key physical properties of these materials remain unexplored—particularly the interplay between magnetic phase stability, electron correlations, and topological band structure. While experimental investigations provide valuable insight into the magnetic transitions and structures of these systems, a systematic comparative theoretical study that includes formation and cohesive energies, magnetic ordering trends, and the effect of electron correlation and SOC is still lacking.

In this work, we perform a comprehensive DFT-based investigation of the structural, electronic, and magnetic properties of XBr_2, XI_2, and XBrI (X = Mn, Co) compounds. We examine the total energies of ferromagnetic and antiferromagnetic phases using GGA and GGA + U approaches, incorporating spin–orbit coupling and analyzing energy–volume curves,

formation energies, and cohesive energies. We also calculate the effective Coulomb screening potential U_{eff} for Mn and Co 3d orbitals and evaluate its effect on the band gap, magnetic moment, and density of states. Furthermore, we identify topological Dirac-like points near the Fermi level in selected Mn-based compounds and analyze their potential for spin-polarized and massless charge transport. This study offers new insights into the electronic correlation effects and topological potential of 3d transition metal halides, contributing to the development of quantum and spintronic materials platforms.

Calculation method

Density functional theory (DFT) is a widely used method for studying and understanding the physical properties of materials. However, for systems containing transition, lanthanide, and actinide elements, the presence of strongly correlated d and f states renders the standard DFT approach within the generalized gradient approximation (GGA) insufficient. This limitation arises from the strong on-site Hubbard interactions, which are not adequately accounted for in conventional GGA. To address this, the DFT + U method is often employed to treat d and f electrons more effectively. The self-interaction correction approach is used to compute the exchange–correlation potential within the GGA + U framework [23, 24].

The results of this work were obtained using DFT as implemented in the WIEN2k computational code [25, 26]. This code solves the Kohn–Sham equations using the full-potential linearized augmented plane wave plus local orbital (APW + lo) method. In the APW + lo method, nonoverlapping muffin-tin spheres are assumed around each atomic position, with the remaining space treated as the interstitial region. Inside the muffin-tin spheres, the Kohn–Sham wave functions, electron charge density, and crystal potential are expanded in terms of spherical harmonics, while in the interstitial region, these quantities are expanded in terms of plane waves. The exchange–correlation potential was evaluated using the generalized gradient approximation (GGA96) [27] within the Perdew–Burke–Ernzerhof (PBE) scheme and the generalized gradient approximation plus Hubbard parameter (GGA + U) method [23, 24, 28].

The GGA + U method is based on atomic-like orbitals and incorporates an orbital-dependent potential characterized by the Coulomb screening parameter U (Hubbard parameter) and the exchange coupling parameter J. The Hubbard parameter (U) for Co and Mn atoms in the GGA + U approach was calculated following the Anisimov and Gunnarsson method. Anisimov and Gunnarsson [28] defined U as the Coulomb energy cost of placing two electrons on the same atomic site. The effective Coulomb screening potential, $U_{\text{eff}} = U - J$, for atoms in solids is directly calculated using ab initio methods. Due to electronic screening effects in the solid-state environment, U_{eff} for an atom in a solid is significantly smaller than its value for the corresponding isolated atom.

Anisimov and Gunnarsson [28] introduced a supercell approach to calculate $U_{\text{eff}} = U - J$. In this method, the number of electrons is varied, and U_{eff} is determined using the following relation:

$$U_{\text{eff}} = \varepsilon_{3d\uparrow}\left(\frac{n+1}{2}, \frac{n}{2}\right) - \varepsilon_{3d\uparrow}\left(\frac{n+1}{2}, \frac{n}{2} - 1\right) - \varepsilon_F\left(\frac{n+1}{2}, \frac{n}{2}\right) + \varepsilon_F\left(\frac{n+1}{2}, \frac{n}{2} - 1\right)$$

Here, n represents the occupation number of the d or f orbitals, such as the 3d electrons of Co and Mn. $\varepsilon_{3d\uparrow}$ denotes the eigenvalue of the 3d electrons with spin-up, and ε_F represents the Fermi level eigenvalue within the GGA approach. All terms in this equation can be calculated using ab initio methods implemented in the WIEN2k package [25, 26]. The first and third terms are computed in one step, while the second and fourth terms are obtained in another step. Thus, these four terms are evaluated using two separate self-consistent calculations within a 2 × 2 × 22 \times 2 \ times 22 × 2 × 2 supercell.

The muffin-tin radii for all atoms were set as $R_{Mn} = R_{Co} = R_{Br} = 2.1$ a.u. and $R_I = 2.2$ a.u. The Kohn–Sham equations were solved in the first Brillouin zone using 4500 k-points, corresponding to a 20 × 20 × 10 mesh. The angular momentum quantum number l_{max} for wave function expansion within the muffin-tin spheres was set to 10, while the wave functions in the interstitial region were expanded up to $K_{max} = 9/R_{MT}(\text{a.u.})^{-1}$, where R_{MT} is the smallest muffin-tin radius in the unit cell. The Fourier expansion cutoff for the charge density and potential in the interstitial region was set to $G_{max} = 14(\text{Ry})^{1/2}$.

All parameters, including the cutoff values and the number of k-points, were chosen to ensure convergence of the forces at atomic positions and the total

energy. The forces were converged to within 0.1 mRy/a.u, and the total energy was converged to 0.00001 Ry.

The WIEN2k code is widely used for studying the physical properties of solids. In this work, the structural optimization, structural parameters, electronic, and magnetic properties of XBr_2, XI_2, and XBrI (X = Mn, Co) compounds were investigated using both GGA and GGA + U approaches. The calculations include the electron density of states, band structures, and total and local magnetic moments for these compounds.

The studied compounds adopt a hexagonal layered van der Waals crystal structure with space group $P\bar{3}m$. The structure features X layers sandwiched between two layers of Br or I atoms. Each central X atom is surrounded by six Br or I atoms positioned at octahedral sites. Calculations were performed for nonmagnetic, ferromagnetic, and antiferromagnetic phases.

For the antiferromagnetic phase, a supercell crystal structure was used, where the spin magnetic moments of X atoms are parallel to the [110] direction. The magnetic moments of X atoms in adjacent cells are aligned antiparallel to one another. In ferromagnetic calculations, the magnetic moments of Mn or Co atoms in cell 1 and cell 2 couple parallel to each other. Conversely, in antiferromagnetic calculations, the magnetic moments of Mn or Co atoms in cell 1 and cell 2 are antiparallel. In the ferrimagnetic phase, all electron moments align parallel to each other. However, in the antiferromagnetic phase, the electron moments in cell 1 and cell 2 couple antiparallel.

Results and discussion

Structural properties

Determining the most stable magnetic ordering and magnetic crystal structure is essential for understanding the behavior of magnetic materials. To identify the stable magnetic crystal structure of Mn and Co-based compounds (XBr_2, XI_2, and XBrI, where X = Mn, Co), total energy calculations were performed at varying unit cell volumes for nonmagnetic, ferromagnetic, and antiferromagnetic phases. For the antiferromagnetic phase, a supercell crystal structure was used. This supercell crystal structure includes two-sublattice antiferromagnet planes perpendicular to the c-axis, where Mn or Co atoms in adjacent alternate layers have spin magnetic moments oriented parallel to the c with opposite direction. The same antiferromagnetic crystal structures are used for these compounds. Therefore, as an example, the antiferromagnetic crystal structure of CoI_2 compound with spin orientation is shown in Fig. 1.

These calculations included SOC within the GGA framework. The compounds were modeled in a hexagonal layered van der Waals structure with space group $P\bar{3}m$. The total energies of the compounds as a function of unit cell volume were fitted using Murnaghan's equation of state. The energy–volume curves for nonmagnetic, ferromagnetic, and antiferromagnetic phases are shown in Fig. 2. The results indicate that all compounds, except $MnBr_2$, exhibit the lowest energy in the antiferromagnetic phase. In contrast, $MnBr_2$ is most stable in the ferromagnetic phase.

The correlation effects associated with Co and Mn 3d electrons near the Fermi energy significantly influence the physical properties of these compounds. The standard GGA approach within density functional theory is insufficient to capture these effects accurately. Consequently, the DFT + U method is a more suitable framework for investigating the physical properties of XBr_2, XI_2, and XBrI compounds.

To better describe the 3d electrons in XBr_2, XI_2, and XBrI (X = Mn, Co) compounds, the effective Coulomb screening potential ($U_{eff} = U - J$) for the 3d orbitals of Mn and Co atoms was calculated using a 2 × 2 × 2 supercell within the Madsen–Novak method [23]. The computed U_{eff} values for these compounds are presented in Table 1. Since there are no theoretical or experimental reports on U and J for these compounds, the calculated U_{eff} values provide new insights. Using these values, the total energy of the compounds was calculated at different unit cell volumes for FM and AFM phases, incorporating spin–orbit coupling within the GGA + U approach. The results, shown in Fig. 2, reveal that the energy–volume curves within GGA + U exhibit higher total energies than the corresponding GGA results, suggesting that GGA is suitable for evaluating energy–volume curves and determining the stability of these compounds.

To solve this problem, we use another formalism of GGA that called GGA-PBEsol approach [29]. The GGA-PBEsol is a suitable approach for predicting stability, structural, and mechanical properties, but usually it is not a suitable for the band gap calculations. Therefore, the total energy of these compounds at different unit cell volumes in AFM phases using GGA-PBEsol + U approach is also calculated. The results of

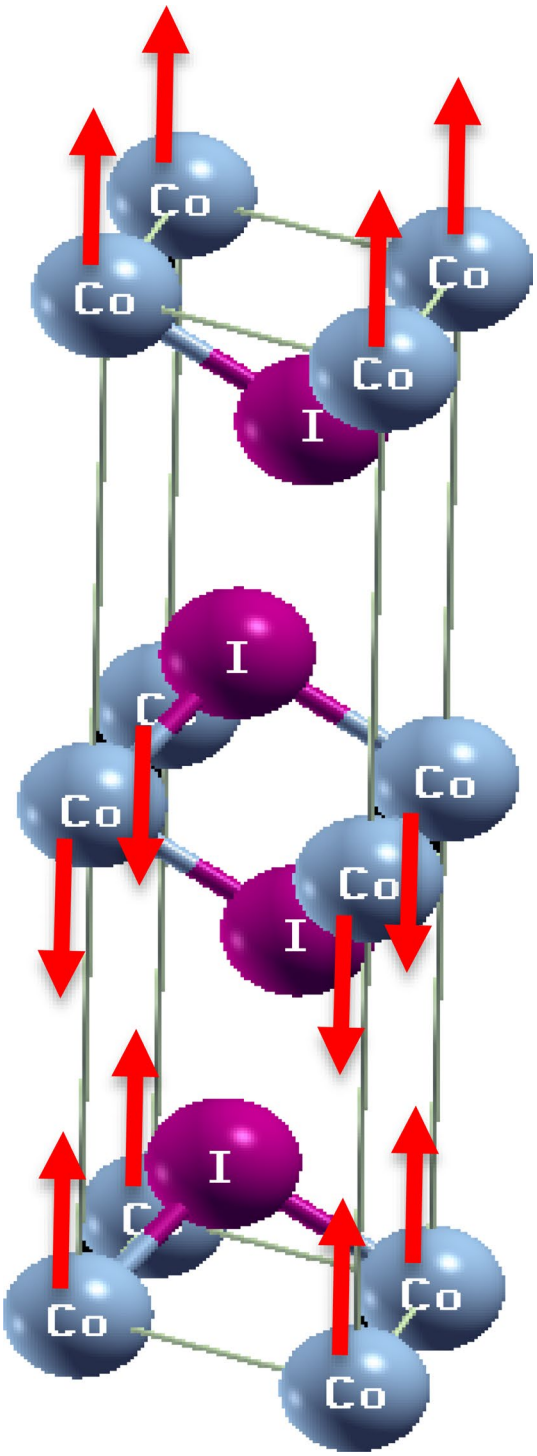

Figure 1 Antiferromagnetic crystal structure of the layered CoI_2 compound under periodic boundary conditions. The magnetic moments on the Co atoms are aligned along the c-axis and exhibit antiparallel orientation between adjacent layers.

this calculation are also given in Fig. 1. These results show that the energy–volume carves of these compounds using GGA-PBEsol + U approach exhibit lower total energies than the corresponding GGA + U results.

The lattice parameters and bulk moduli of the compounds in FM and AFM phases, calculated using GGA, GGA + U, and GGA-PBEsol + U (in AFM phase), are compared with available reported results [2, 9, 14–16, 20, 30–32] in Table 2. The calculated values show acceptable agreement with previously reported data. The lattice parameters are influenced by the size of the constituent atoms and bonding strength in the solid. While the atomic size increases along a row of the periodic table, the bonding strength also increases, but to a greater extent. Consequently, the lattice parameters of Mn-based compounds are larger than those of Co-based compounds due to the effect of bonding strength.

The bulk modulus, a key indicator of material stiffness, is primarily influenced by the degree of covalency and ionicity in the bonding. Increased covalency strengthens bonds and raises the bulk modulus, while higher ionicity reduces bonding charge density, thereby lowering the bulk modulus. The compounds XBr_2, XI_2, and XBrI (X = Mn, Co) exhibit varying degrees of covalent and ionic bonding. The calculated bulk moduli indicate an increasing trend along the series from $MnBr_2$, MnI_2, and MnBrI to $CoBr_2$, CoI_2, and CoBrI, attributed to increased covalency and reduced ionicity.

To compare the ground-state total energy of these compounds in FM and AFM phases, the energy difference ($\Delta E = E_{AFM} - E_{FM}$) was calculated. The results, presented in Table 1, indicate that $\Delta E > 0$ corresponds to FM stability, while $\Delta E < 0$ signifies AFM stability. The calculated values show that all compounds except $MnBr_2$ are more stable in the AFM phase. For MnBrI, the small ΔE magnitude within GGA suggests that it exhibits weak antiferromagnetic behavior.

Before analyzing the electronic and magnetic properties of these compounds, their energy stability was investigated by calculating their formation and cohesive energies. The cohesive energy (E_C) of XYZ (X = Mn, Co; Y, Z = Br, I) compounds is determined using equation [33–35]:

$$E_C = \frac{E_{Bulk}^{total}(XYZ) - N_X E_X^{total} - N_Y E_Y^{total} - N_Z E_Z^{total}}{N_X + N_Y + N_Z} \quad (1)$$

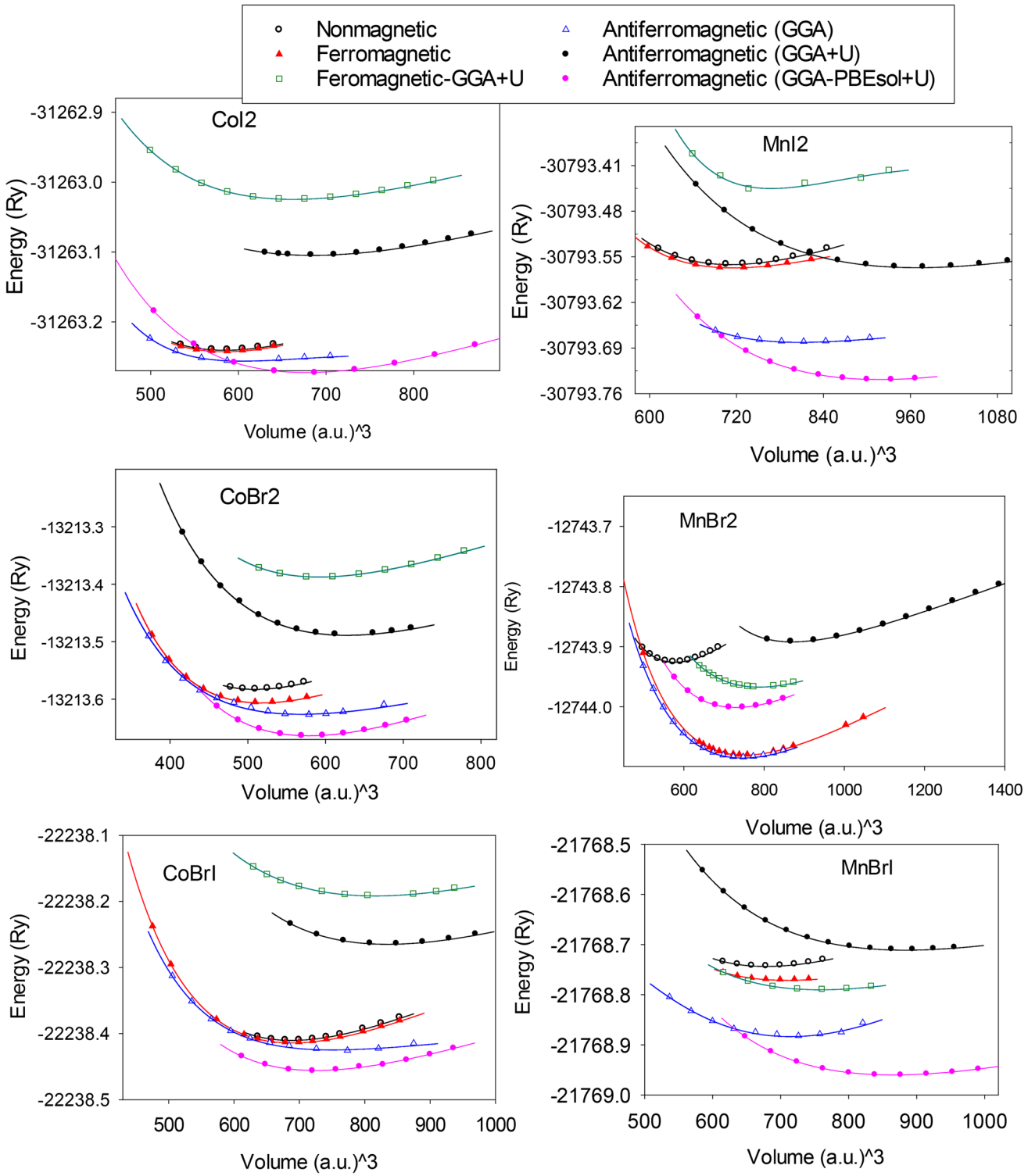

Figure 2 The calculated total energy–volume curves of XBr_2, XI_2, and XBrI (X = Mn, Co) compounds in nonmagnetic, ferromagnetic, antiferromagnetic phases and GGA-PBEsol + U (in AFM phase), including SOC, are shown for both GGA and GGA + U approaches.

where $E_{\text{Bulk}}^{\text{total}}(XYZ)$ is the total energy per formula unit of the compound, E_X^{total}, E_Y^{total}, and E_Z^{total} are the total energies of the individual X, Y, and Z atoms, respectively, and N_X, N_Y, and N_Z are the numbers of X, Y and Z atoms in the cell.

Table 1 The calculated $U_{eff} = U - J$ for Mn and Co 3d orbitals in XBr_2, XI_2, and XBrI (X = Mn, Co) compounds, the total energy difference (($\Delta E = E_{AFM} - E_{FM}$) between FM and AFM phases within the GGA approach, and the cohesive and formation energies of these compounds in FM and AFM phases calculated using GGA and GGA + U approaches

			$MnBr_2$	MnI_2	MnBrI	$CoBr_2$	CoI_2	CoBrI
U_{eff}(eV)	This work		5.85	5.30	7.07	5.17	5.69	5.70
	Other reports			4 [8]				
$\Delta E = E_{AFM} - E_{FM}$(mRy)	GGA		0.55	− 109.82	− 0.52	− 14.70	− 4.09	− 5.95
Formation energies (mRy/atom)	FM	GGA	− 19.39	− 1.99	− 13.93	− 65.06	− 10.78	− 2.29
		GGA + U	− 7.82	3.60	4.93	15.59	21.87	20.16
	AFM	GGA	− 16.35	− 8.98	− 14.01	− 79.67	− 14.60	− 3.01
		GGA + U	− 0.98	2.71	− 3.54	− 60.44	14.22	13.28
Cohesive energies (mRy/atom)	FM	GGA	− 63.64	− 39.59	− 30.61	− 68.07	− 59.37	− 62.52
		GGA + U	− 52.06	− 35.18	15.61	− 45.97	− 37.01	− 40.58
	AFM	GGA	− 61.59	− 50.57	− 32.53	− 69.53	− 60.95	− 63.13
		GGA + U	− 44.15	− 38.86	2.08	− 55.52	− 44.66	− 46.93

Table 2 The calculated lattice parameters and bulk moduli of XBr2, XI2, and XBrI (X = Mn, Co) compounds in FM and AFM phases using GGA, GGA + U, and GGA-PBEsol + U (in AFM phase) approaches, compared with available reported results [2, 8, 9, 14, 16, 19, 20, 30–32]

	Compounds	MnI_2	$MnBr_2$	$CoBr_2$	CoI_2	CoBrI	MnBrI
a(Å)	FM (GGA)	4.0060	4.0755	3.4646	3.70479	3.7943	4.0519
	FM (GGA + U)	4.1093	4.1198	3.65375	3.79859	3.99907	4.1042
	AFM (GGA)	4.1630	3.9282	3.5394	3.7259	3.911	4.0064
	AFM (GGA + U)	4.218	4.2390	3.6794	3.8196	4.0242	4.3177
	AFM (GGA-BEsol + U)	4.3561	4.0548	3.7213	3.9147	3.8623	4.2903
	Other reported results	4.148 [2] 4.146 [30], 4.17 [31] 4.159 [32],	3.873 [2] 3.868[20] 3.855 [32], 3.87[31]	3.680 [15] 3.738 [16], 3.74 [31]	3.985 [9] 3.974 [14], 3.89 [31]	–	–
C (Å)	FM (GGA)	6.4929	6.6839	6.3714	6.45041	7.07275	6.5763
	FM (GGA + U)	6.7556	6.8388	6.54021	6.78048	7.51825	6.6245
	AFM (GGA)	6.7857	6.4029	6.6894	6.3714	7.3139	6.5705
	AFM (GGA + U)	7.0018	7.1640	6.8437	6.9135	7.6057	6.9946
	AFM (GGA-BEsol + U)	7.1659	6.5749	6.1888	6.5464	7.20321	6.9632
	Other reported results	6.837 [2] 6.829 [30], 7.15 [31]	6.271 [2] 6.272[20], 6.48[31]	6.120 [15] 6.41 [31]	6.664 [9] 6.636 [14], 6.63 [31]	–	–
c/a	FM (GGA)	1.648	1.64	1.839	1.7438	1.864	1.623
	FM (GGA + U)	1.65	1.66	1.79	1.785	1.88	1.614
	AFM (GGA)	1.63	1.68	1.89	1.71	1.87	1.64
	AFM (GGA + U)	1.66	1.69	1.86	1.81	1.89	1.62
Bulk modulus (GPa)	FM (GGA)	32.58	28.42	48.40	41.61	37.63	28.43
	FM (GGA + U)	21.81	26.45	37.46	30.21	20.54	26.97
	AFM (GGA)	22.84	28.57	26.03	24.38	17.56	45.30
	AFM (GGA + U)	20.24	21.91	36.13	27.79	24.74	23.02
		23.35	29.92	41.21	33.52	25.87	24.40

The formation energy (ΔH_f) of XYZ compounds is calculated using the equation:

$$\Delta H_f(XYZ) = E^{total}(XYZ) - N_X E^{total}(X) - N_Y E^{total}(Y) - N_Z E^{total}(Z) \quad (2)$$

where $E^{total}(XYZ)$ is the ground-state energy per formula unit of the compound, and $E^{total}(X)$, $E^{total}(Y)$ and $E^{total}(Z)$ are the ground-state energies per atom of the pure X, Y, and Z elements.

The cohesive and formation energies of XBr_2, XI_2, and XBrI (X = Mn, Co) compounds were calculated in both ferromagnetic and antiferromagnetic phases using GGA and GGA + U approaches, and the results are summarized in Table 1. The calculations indicate that all compounds, except $MnBr_2$, are more stable in the antiferromagnetic phase, whereas $MnBr_2$ exhibits slightly greater stability in the ferromagnetic phase. The small energy difference between the two phases for $MnBr_2$ highlights its near-degenerate magnetic states. The more negative cohesive and formation energies signify greater stability of the materials [36]. The results also show that XBr_2 is more stable than XBrI and XI_2 for both Mn- and Co-based compounds.

The positive cohesive and formation energy values obtained within the GGA + U approach, along with the energy–volume curves previously discussed, suggest that this approach is not ideal for structural calculations or phase stability studies. However, GGA + U proves useful for accurately describing the distribution of d electrons, thereby improving calculations of electronic and magnetic properties.

Electronic properties

Electronic density of states

The total and partial electron density of states (DOS) of XBr_2, XI_2, and XBrI (X = Mn, Co) compounds were calculated in their most magnetically stable phases using the GGA and GGA + U approaches. The total DOS for these compounds is shown in Fig. 3. Comparing the DOS reveals that the effective Coulomb screening potential (U_{eff}) has a considerable impact on the 3d electron distribution of Co and Mn atoms. The energy band gap in FM and AFM phases increases when U_{eff} is included within the GGA + U framework. For MnI_2 in the AFM phase, the calculated DOS within GGA + U aligns well with previously reported results [8].

The energy band gaps for spin-up and spin-down electrons in the FM and AFM phases of these compounds, calculated using GGA and GGA + U with SOC, are provided in Table 3 and compared with reported results [31, 37]. The energy band gap near the Fermi energy in the AFM phase, except for CoI_2 and $CoBr_2$, originates from the Mn and Co atoms, indicating the presence of an AFM gap. In $MnBr_2$, MnI_2, and CoBrI, the DOS at the Fermi energy in the FM phase calculated within GGA suggests metallic behavior. However, in the AFM phase, except for CoI_2, the inclusion of U_{eff} within GGA + U leads to the opening of an energy band gap, resulting in semiconducting behavior.

In order to understand the effect of U_{eff} on the energy band gap of these compounds, the energy band gap of these compounds in the two ferromagnetic and antiferromagnetic phases is calculated using different values of U_{eff}. The results of this calculation are given in Fig. 4. These results show that the energy band gap of these compounds in the two ferromagnetic and antiferromagnetic phases, except for $MnBr_2$, $MnCo_2$ and CoI_2 compounds in antiferromagnetic phase, increases with increase in value of U_{eff}. The weight of this increase is different for different compounds and different U_{eff}. The energy band gap of CoI_2 compound in the antiferromagnetic phase is zero and does not change with increase in U_{eff}. Therefore, this compound is metal for all U_{eff} values. The energy band gap of $MnBr_2$ and $MnCo_2$ compounds in the antiferromagnetic phase decreased and has minimum values for U_{eff} = 4.8 and U_{eff} = 3.4 eV, respectively. After further increment in U_{eff}, the energy band gap starts increasing.

For the ferrimagnetic phase of $MnBr_2$ within GGA + U, as well as $CoBr_2$ and CoI_2 within GGA, the compounds exhibit half-metallic behavior due to the presence of a band gap in the spin-up or spin-down DOS. The calculated energy band gap in the AFM phase for these compounds agrees more closely with reported results [31].

To further examine the effect of U_{eff} on the electronic properties, the partial DOS of Co and Mn atoms in their most stable magnetic phases (AFM for all compounds except $MnBr_2$, which is a FM) using GGA + U with deferent values of U_{eff} approach, is shown in Fig. 5. The results indicate that U_{eff} significantly influences the electronic properties of Co and Mn atoms. By adding U_{eff} within the GGA + U approach, the band gap between the occupied and

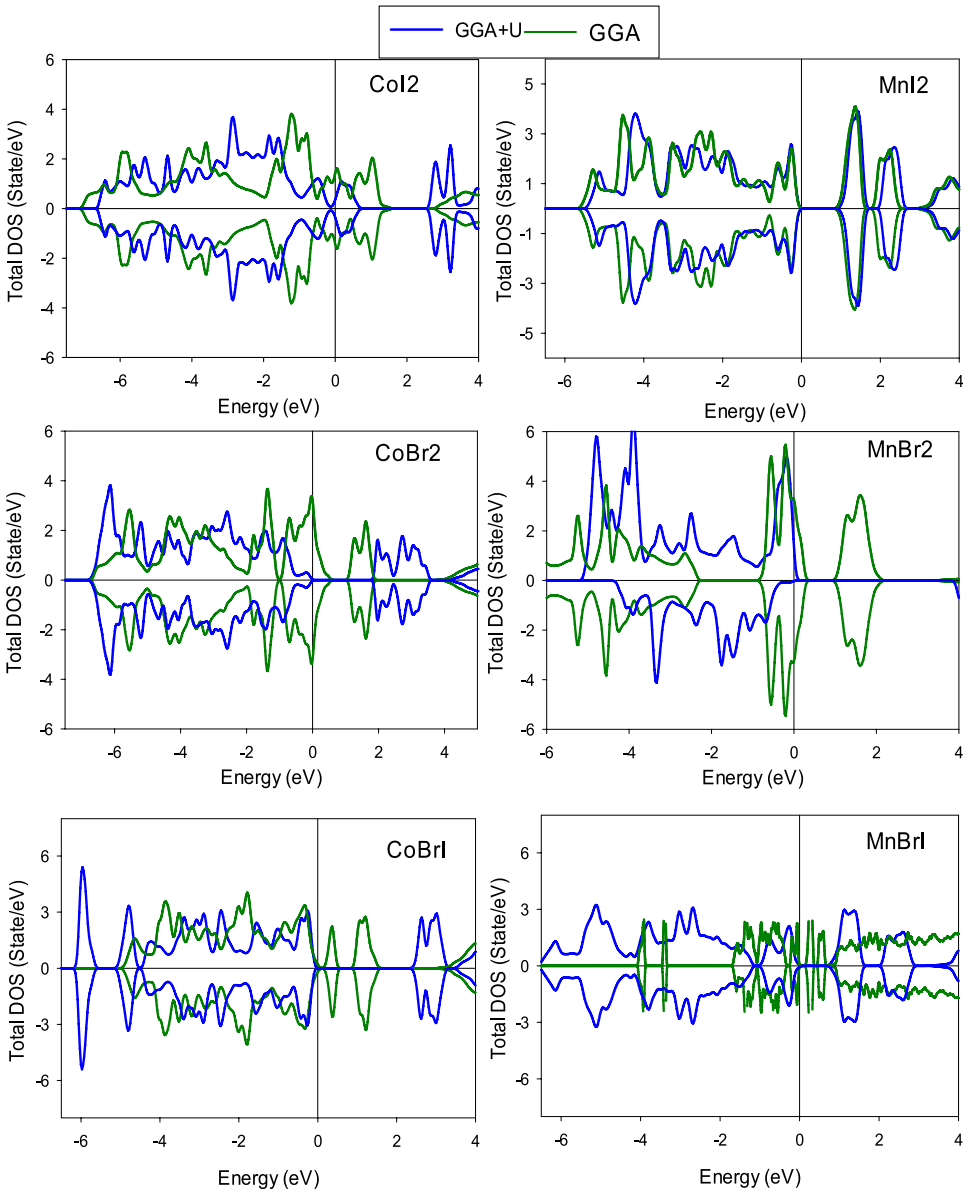

Figure 3 Total electronic density of states (DOS) for XBr_2, XI_2, and XBrI (X = Mn, Co) compounds, calculated in their most stable magnetic phases (antiferromagnetic for all compounds except $MnBr_2$, which is ferromagnetic) using both GGA and GGA + U approaches. The vertical line at zero energy indicates the Fermi level.

Table 3 The calculated energy band gaps (in eV) of XBr_2, XI_2, and XBrI (X = Mn, Co) compounds in FM and AFM phases using GGA and GGA + U approaches, along with available reported results

Compounds	MnI_2		$MnBr_2$		MnBrI		CoI_2		$CoBr_2$		CoBrI	
	up	dn	up	dn	up	dn	up	dn	up	dn	up	dn
Ferromagnetic (GGA)	0	0	0	0	2.74	2.74	0	0.704	3.99	0	0	0
Ferromagnetic (GGA + U)	1.97	2.80	0	3.81	3.01	3.01	2.63	1.06	4.67	2.26	3.61	2.17
Antiferromagnetic (GGA)	1.07	1.07	1.52	1.52	0.144	0.144	0	0	0	0	0.17	0.17
Antiferromagnetic (GGA + U)	1.09	1.09	1.79	1.79	0.701	0.701	0	0	1.87	1.87	2.464	2.464
Other work	1.17 [31]		1.60 [31]		–		0 [31]		0.11 [310]		–	

Notably, energy gaps of 2.35 eV [37] and 0.2 eV [16] have been reported for the $CoBr_2$ monolayer

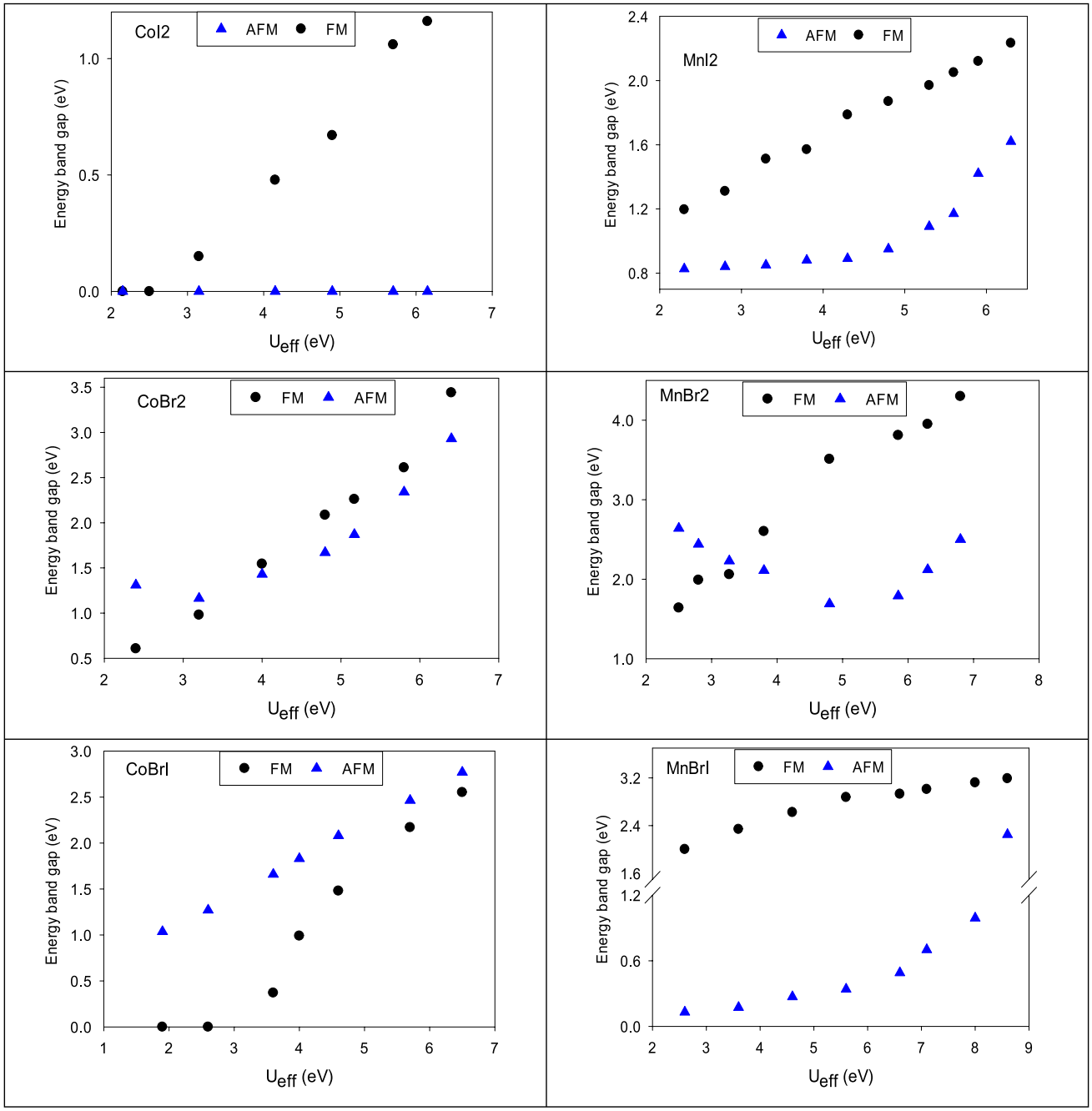

Figure 4 Variation of the energy band gap for XBr_2, XI_2, and XBrI (X = Mn, Co) compounds in the AFM and FM phases, calculated using the GGA + U approach with different values of the effective Coulomb interaction U_{eff}.

empty 3d orbitals of Mn and Co atoms, particularly in the majority spin channel, increases due to enhanced localization of the 3d orbitals. The peaks located above the Fermi energy are shifted toward the higher energy region with increase in value of U_{eff}. Furthermore, the peaks of the electron density of states between − 4 and − 6 eV, which are due to the d orbital of Co or Mn atom, are shifted by changing the value of U_{eff}. The primary magnetic properties of these compounds are predominantly determined by the Mn and Co atoms.

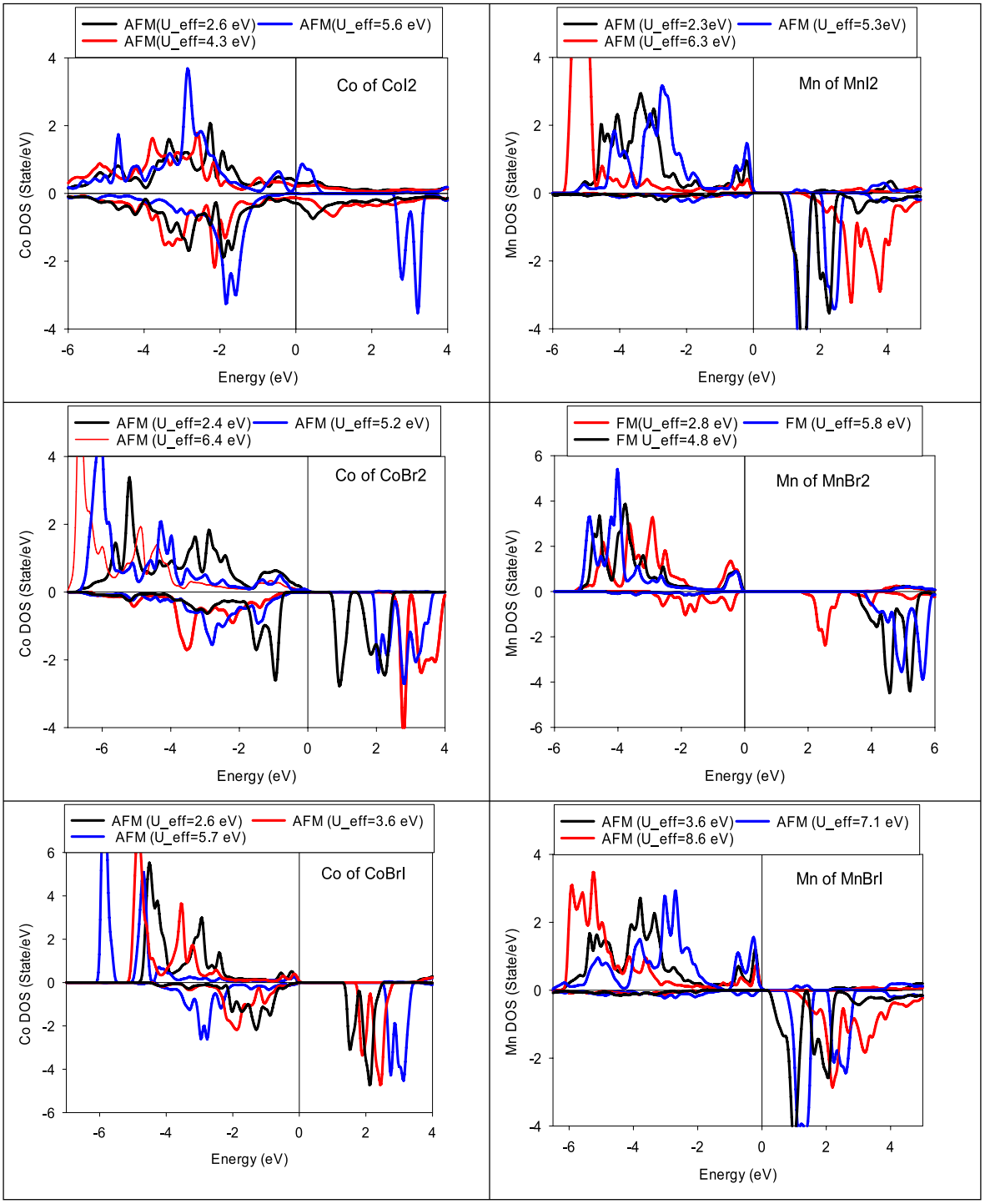

Figure 5 Partial density of states for Co and Mn atoms in XBr_2, XI_2, and XBrI (X = Mn, Co) compounds, calculated in their most stable magnetic phases (antiferromagnetic for all compounds except $MnBr_2$, which is ferromagnetic) using the GGA + U approach with different values of the effective Coulomb interaction U_{eff}. The vertical line at zero energy denotes the Fermi level.

Topological Dirac point in band structure

Two- and three-dimensional topological materials exhibit unique edge and surface states, respectively, which enable the development of novel quantum states and practical applications [38, 39]. Topological Weyl and Dirac points are significant features of such materials, characterized by their distinct properties arising from the interaction of valence and conduction bands near the Fermi energy. At these points, the bands cross each other with linear energy dispersion, leading to massless fermions with opposite chirality (left- or right-handed), analogous to the Berry curvature field. The presence of Weyl or Dirac points can be identified through calculated band structures [38, 40–42].

The band structures of XBr_2, XI_2, and XBrI (X = Mn, Co) compounds in FM and AFM phases were calculated within GGA and GGA + U, including SOC. The Dirac points were investigated by analyzing the band structures near the Fermi energy. The calculated band structures of $MnBr_2$, MnI_2, and MnBrI in the AFM phase using GGA + U with SOC are shown in Fig. 6. The results indicate the presence of topological Dirac-like points between the *R* and Γ points, with band openings of 6.3 meV, 7.8 meV, and 6.9 meV, respectively. In contrast, no topological Dirac points were found in the band structures of $CoBr_2$, CoI_2, or CoBrI in either FM or AFM phases within GGA or GGA + U.

The Dirac-like points in $MnBr_2$, MnI_2, and MnBrI result in massless fermions between the *R* and Γ points, which contribute to phenomena such as the quantum Hall effect, magnetoelectric coupling, and ultra-high carrier mobility. Additionally, band inversion near the Γ point in a monolayer of $CoBr_2$ within GGA + U with small Hubbard parameters (less than 1 eV) has been reported [15]. For larger U, the band inversion disappears, indicating that the topological properties of $CoBr_2$ are sensitive to the magnitude of U.

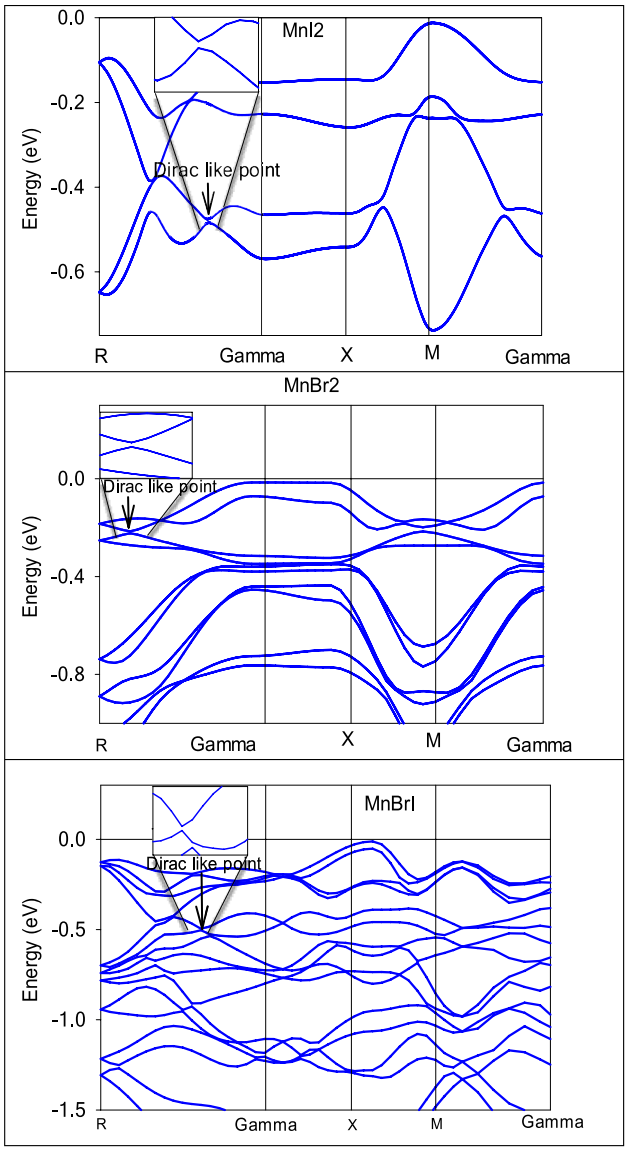

Figure 6 The calculated band structures of $MnBr_2$, MnI_2, and MnBrI compounds in antiferromagnetic phase within GGA + U approach near the fermi energy. To make the Dirac-like point more clearly visible, the band structures are shown near the Fermi energy for excited states (below the Fermi energy).

Magnetic properties

The magnetic properties of XBr_2, XI_2, and XBrI (X = Mn, Co) compounds were investigated by calculating their total and local magnetic moments in ferromagnetic and antiferromagnetic phases using GGA and GGA + U approaches. The results, presented in Table 4, are compared with previously reported values.

The calculated local magnetic moment at Co or Mn sites, except for $CoBr_2$ in the magnetic phase, increases when the effective Coulomb screening potential is included within the GGA + U framework. For Mn-based compounds ($MnBr_2$, MnI_2, and MnBrI), the Mn local magnetic moment is generally larger than the corresponding Co local magnetic moment, except for

Table 4 The calculated total and local magnetic moments of XBr_2, XI_2, and XBrI (X = Mn, Co) compounds in FM and AFM phases using GGA and GGA + U approaches, along with available reported results

Compounds		MnI_2	Mn_2Br	$CoBr_2$	CoI_2	CoBrI	MnBrI
Magnetic moment at Mn or Co atomic position (μ_B/Co)	Ferromagnetic (GGA)	0.99	0	3.15	0.95	0.05	4.11
	Ferromagnetic (GGA + U)	4.33	4.48	2.58	2.41	2.60	4.30
	Antiferromagnetic (GGA)	4.08	4.37	1.75	0.92	2.35	4.14
	Antiferromagnetic (GGA + U)	4.41	4.59	2.58	1.30	2.67	4.43
	Other work	–	–	–	1.67 [9], 2.16 [9]	–	–
Total magnetic moment (μ_B)	Ferromagnetic (GGA)	4.97	0	4.05	1.01	0.05	4.99
	Ferromagnetic (GGA + U)	4.99	4.99	2.98	2.98	2.99	4.99
	Other work	4.51 [22], 5.00 [31]	4.52 [22], 5[31]	2.49 [22], 3 [15], 3 [31]	1.67 [10], 1.01 [31]	–	–

The total magnetic moments in the AFM phase are not included due to their zero values. Notably, a Co local magnetic moment of 2.67 μB has been reported for the $CoBr_2$ monolayer [37]

$MnBr_2$ in the FM phase within GGA, where the magnetic moment is zero.

The magnetic moment of these compounds mainly arises from Co or Mn atoms, while Br and I have little contribute to the magnetic moment. Therefore, to find the effect of effective Coulomb screening potential on the magnetic moment of these compounds in the two ferromagnetism and antiferromagnetic phases, the Mn or Co local magnetic moment of these compounds is calculated and the results are shown in Fig. 7. These carves show that the effect of U_{eff} on magnetic moments of these compounds is small. The magnetic moment of these compounds, except for $CoBr_2$ compound in ferromagnetic phase, small increases with increase in U_{eff}. The magnetic moment of $CoBr_2$ compound in the ferromagnetic phase first small increases and then small decreases with increase in U_{eff}. Comparing the graphs of Fig. 7 with 5 shows that the effect of U_{eff} on the energy gap of these compounds is greater than the magnetic moment.

The magnetic moments of XBr_2 and XI_2 in their most stable magnetic phases calculated within GGA + U are in acceptable agreement with reported results. The inclusion of the effective Coulomb screening potential enhances the calculated magnetic moments of XBr_2, XI_2, and XBrI compounds, improving the description of their magnetic properties.

Conclusion

The investigation of XBr_2, XI_2, and XBrI (X = Mn, Co) compounds using density functional theory with GGA and GGA + U approaches provided a comprehensive understanding of their structural, electronic, and magnetic properties. The analysis of energy stability, supported by cohesive and formation energy calculations, demonstrated that all compounds except $MnBr_2$ are energetically more stable in the antiferromagnetic phase. For $MnBr_2$, the ferromagnetic phase exhibited marginally greater stability. The results highlighted that the inclusion of the effective Coulomb screening potential within the GGA + U framework is crucial for improving the description of electronic and magnetic properties, although it is less suitable for structural stability studies.

The electronic properties revealed significant effects of U_{eff} on the density of states and energy band gaps. Most compounds, except CoI_2 in the antiferromagnetic phase, transitioned to semiconducting behavior upon incorporating U_{eff} within the GGA + U approach. Additionally, the ferrimagnetic phase of $MnBr_2$ in GGA + U, along with $CoBr_2$ and CoI_2 in GGA, exhibited half-metallic behavior due to the presence of a spin-polarized energy band gap. In the antiferromagnetic phase, $MnBr_2$, MnI_2, and MnBrI displayed

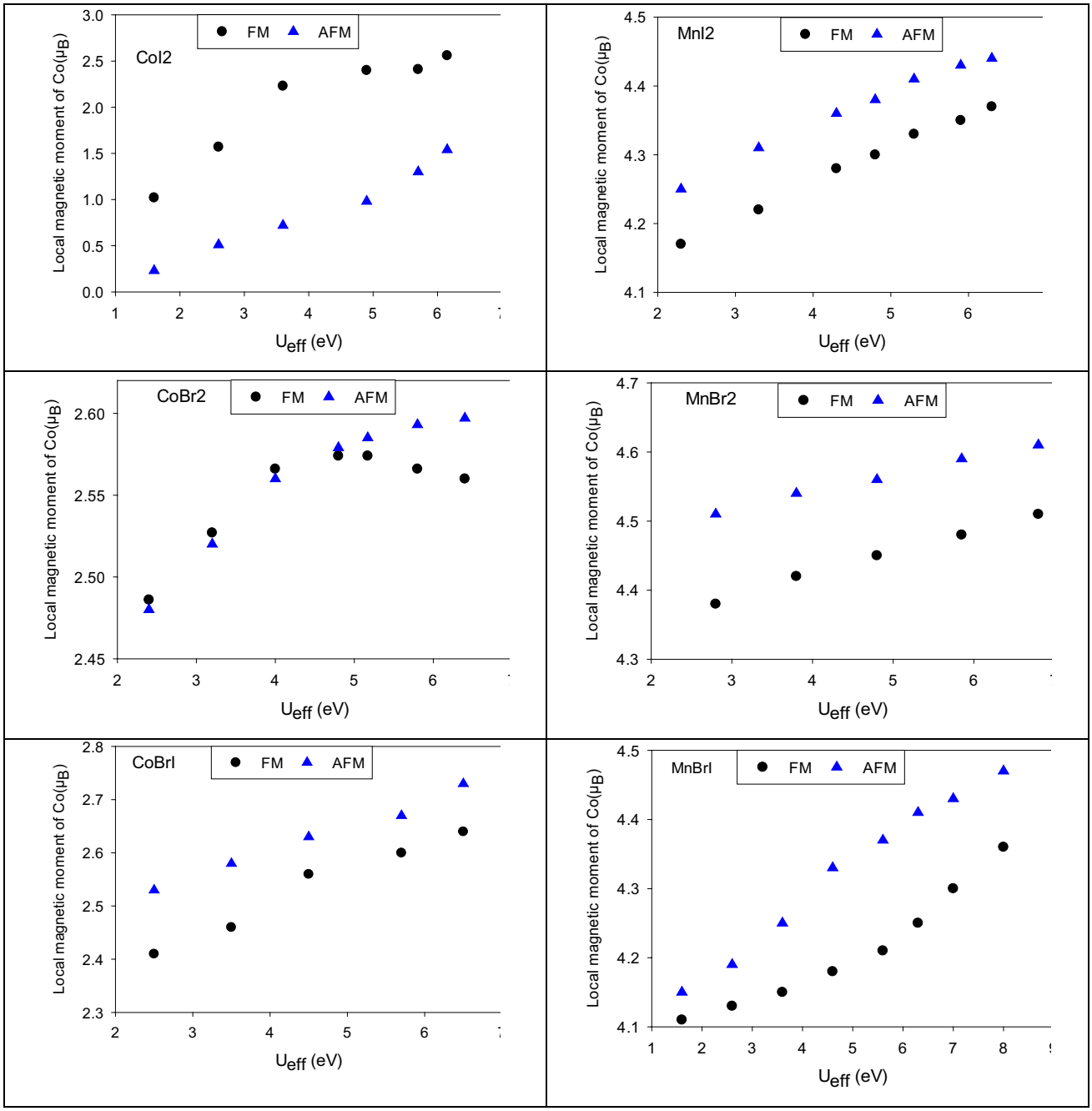

Figure 7 Local magnetic moment of the Co or Mn atom in XBr_2, XI_2, and XBrI (X = Mn, Co) compounds, calculated for AFM and FM phases using the GGA + U approach with different values of the effective Coulomb interaction U_{eff}.

topological Dirac-like points between the *R* and Γ points, signifying massless fermions and associated quantum phenomena such as quantum Hall effects and ultra-high carrier mobility. The absence of Dirac points in $CoBr_2$, CoI_2, and CoBrI highlights the distinct role of Mn atoms in realizing such topological features.

The magnetic properties, characterized by total and local magnetic moments, revealed a consistent enhancement of magnetic moments with the inclusion of U_{eff}, particularly at Mn and Co sites. The results demonstrated acceptable agreement with available reported values, further validating the computational approach. The magnetic moment of these compounds

in their most stable phases small increases with increase in U_{eff}.

The observed semiconducting, half-metallic, and topological behaviors, along with enhanced magnetic moments, highlight the potential of Mn- and Co-based van der Waals compounds for applications in quantum and spintronic devices.

Acknowledgements

DV acknowledges funding support from the National Science Foundation (NSF) under grant number CBET-2110603.

Author contributions

Al-Suwaychit Fadhil Noori Yaqoob was involved in investigation, methodology, data curation, formal analysis, writing—original draft preparation. Zahra Nourbakhsh helped in supervision, conceptualization, validation, formal analysis, resources, writing—reviewing and editing. Daryoosh Vashaee contributed to supervision, validation, formal analysis, funding acquisition, writing—reviewing and editing.

Data availability

The datasets generated and analyzed during the current study are not publicly available due to their extensive size and complexity. However, they are available from the corresponding author upon reasonable request and with sufficient notice.

Declarations

Conflicts of interest The authors declare that they have no conflicts of interest.

Ethical approval Not applicable.

References

[1] Li Y, Chen D, Dong X, Qiao L, He Y, Xiong X, Li J, Peng X, Zheng J, Wang X, Li X, Wang Q, Duan J, Wang Z, Han J, Xiao W (2020) Magnetic and electric properties of single crystal MnI_2. J Phys: Condens Matter 32:335803

[2] Ronda CR, Siekman HH, Haas C (1987) Photoluminescence and absorption of $MnCI_2$, $MnBr_2$ and MnI_2. Physica 144B:331

[3] Hoekstra HJWM, Boudwijn PR, Groenier H, Haas C (1983) Optical absorption and magnetic circular dichroism of MI_2. Physica B 121:62

[4] Hoekstra HJ, Folkersma HF, Haas C (1985) Optical absorption and magnetic circular dichroism of $MnBr_2$. Phys B 128:133

[5] Sato T, Kadowaki H, Iio K (1995) Successive phase transitions in the hexagonal-layered Heisenberg antiferromagnets MnX_2 (X – Br, I). Phys B 213:224

[6] Kurumaji T, Seki S, Ishiwata S, Murakawa H, Tokunaga Y, Kaneko Y, Tokura Y (2011) Magnetic-field induced competition of two multiferroic orders in a triangular-lattice helimagnet MnI_2. Phys Rev Lett 106:167206

[7] Wu X, Cai Y, Xie Q, Weng H, Fan H, Hu J (2012) Magnetic ordering and multiferroicity in MnI_2. Phys Rev B 86:134413

[8] Van Erk W, Haas C (1975) Optical absorption of MnI_2. Phys Status Solidi (b). 70:517

[9] Kuindersma SR, Sanchez JP, Haas C (1981) Magnetic and structural investigations on NiI_2 and CoI_2. Physica B + C 111:231

[10] Friedt JM, Sanchez JP, Shenoy GK (1976) Electronic and magnetic properties of metal diiodides MI_2 (M = V, Cr, Mn, Fe Co, Ni, and Cd) from 1291Mossbauer spectroscopy. J Chem Phys 65:5093

[11] Kurumaji T, Seki S, Ishiwata S, Murakawa H, Kaneko Y, Tokura Y (2013) Magnetoelectric responses induced by domain rearrangement and spin structural change in triangular-lattice helimagnets NiI_2 and CoI_2. Phys Rev B 87:014429

[12] Chen AL, Yu PY (1994) Near-IR absorption measurements of the transition-metal iodides under pressure. In: American Institute of Physics, conference proceeding

[13] Stener E, Pastemak MP (1992) High Pressure Research 1992, Gordon and Breach Science Publishers S.A., United Kingdom

[14] Mekata M, Kuriyama H, Ajiro Y, Mitsuda S, Yoshizawa H (1992) First-order magnetic transition in CoI_2. J Magn Magn Mater 104:859

[15] Chen P, Zou J-Y, Liu B-G (2017) Intrinsic ferromagnetism and quantum anomalous Hall effect in a $CoBr_2$ monolayer. Phys Chem Chem Phys 19:13432

[16] Banerjee H, Aichhorn M (2021) Importance of electronic correlations for the magnetic properties of the two-dimensional ferromagnet $CoBr_2$. Phys Rev B 103:195123

[17] Lockwood DJ, Mischler G, Schmidt MC, Johnstone IW (1979) Raman scattering from electronic excitations and phonons in paramagnetic and antiferromagnetic $CoBr_2$. J Phys C: Solid State Phys 12:1955–1975. https://doi.org/10.1088/0022-3719/12/10/025

[18] Regis M, Farge Y, Royce BS (1976) Optical studies of the magnetic phase diagram of $MnCl_2$ and $MnBr_2$. In: AIP Conference Proceedings, vol 29. no 1, pp 654-655. American Institute of Physics

[19] Sakisaka Y (1975) Optical absorption spectra of $MnCl_2$ and $MnBr_2$. J Phys Soc Japan 38(2):505–508

[20] Wollan EO, Koehler WC, Wilkinson MK (1958) Neutron diffraction study of the magnetic properties of $MnBr_2$. Phys Rev 110:638

[21] Hoekstra HJWM, Folkersma HF, Haas C (1984) Exciton dispersion in MnI_2 and $MnBr_2$. Solid State Commun 51:657–661

[22] Yekta Y, Hadipour H, Şaşıoğlu E, Friedrich C, Jafari SA, Blügel S, Mertig I (2021) Strength of effective Coulomb interaction in two-dimensional transition-metal halides MX2 and MX3 (M= Ti, V, Cr, Mn, Fe Co, Ni; X= Cl, Br, I). Phys Rev Mater 5:034001

[23] Madsen GKH, Novák P (2005) Charge order in magnetite An LDA + U study. Europhys Lett 69:777

[24] Anisimov VI, Solovyev IV, Korotin MA, Czyzyk MT, Sawatzky GA (1993) Density-functional theory and NiO photoemission spectra. Phys Rev B 48:16929

[25] Schwarz K, Blaha P, Madsen GKH (2002) Electronic structure calculations of solids using the WIEN2k package for material sciences. Comput Phys 147:71

[26] Perdew JP, Burke K, Ernzerhof M (1996) Generalized gradient approximation made simple. Phys Rev Lett 77:3865

[27] Blaha P, Schwarz K, Madsen GKH, Kvasnicka D, Luitz J (2010) WIEN2k: an augmented plane wave+local orbitals program for calculating crystal properties. Vienna University of Technology, Austria

[28] Anisimov VI, Gunnarsson O (1991) Density-functional calculation of effective Coulomb interactions in metals. Phys Rev B 43:7570

[29] Perdew JP, Ruzsinszky A, Csonka GI, Vydrov OA, Scuseria GE, Constantin LA, Zhou X, Burke K (2008) Restoring the density-gradient expansion for exchange in solids and surfaces. Phys Rev Lett 100:136406

[30] Cable JW, Wilkinson MK, Wollan EO, Koehler WC (1962) Neutron diffraction investigation of the magnetic order in MnI_2. Phys Rev 125:1860

[31] The Materials Project site. https://next-gen.materialsproject.org

[32] Luo J, Xiang G, Tang Y, Ou K, Chen X (2020) The electric and magnetic properties of novel two-dimensional $MnBr_2$ and MnI_2 from first-principles calculations. J Appl Phys 128:113901

[33] Kingsbury RS, Rosen AS, Gupta AS, Munro JM, Ong SP, Jain A, Dwaraknath S, Horton MK, Persson KA (2022) A flexible and scalable scheme for mixing computed formation energies from different levels of theory. npj Comput Mater 8:195

[34] Tenelanda-Osorio LI, Vélez ME (2021) First principles study of the thermodynamic, mechanical and electronic properties of crystalline phases of chromium nitrides. J Phys Chem Solids 148:109692

[35] De Jong M, Chen W, Angsten T, Jain A, Notestine R, Gamst A, Sluiter M, Krishna Ande C, Van Der Zwaag S, Plata JJ, Toher C (2015) Charting the complete elastic properties of inorganic crystalline compounds. Sci Data 2:1–3

[36] Ullah R, Ali MA, Murtaza G, Khan A, Mahmood A (2020) "Ab initio study for the structural, electronic, magnetic, optical, and thermoelectric properties of K_2OsX_6 (X = Cl, Br) compounds. Int J Energy Res 44:9035

[37] Lv HY, Lu WJ, Luo X, Zhu XB, Sun YP (2019) Strain- and carrier-tunable magnetic properties of a two-dimensional intrinsically ferromagnetic semiconductor: $CoBr_2$ monolayer. Phys Rev B 99:134416

[38] Yan B, Felser C (2017) Topological materials: Weyl semimetals. Annual Rev Condens Matter Phys 8:337

[39] Armitage NP, Mele EJ, Vishwanath A (2018) Weyl and Dirac semimetals in three-dimensional solids. Rev Mod Phys 90:015001

[40] Lv BQ, Weng HM, Fu BB, Wang XP, Miao H, Ma J, Richard P, Huang XC, Zhao LX, Chen GF, Fang Z, Dai X, Qian T, Ding H (2015) Discovery of a Weyl fermion semimetal and topological Fermi arcs. Phys Rev X 5:031013

[41] Liu ZK, Yang LX, Sun Y, Zhang T, Peng H, Yang HF, Chen C, Zhang YF, Guo YF, Prabhakaran D, Schmidt M (2016) Evolution of the Fermi surface of Weyl semimetals in the transition metal pnictide family. Nat Mater 15:27

[42] Polash MMH, Yalameha S, Zhou H, Ahadi K, Nourbakhsh Z, Vashaee D (2021) Topological quantum matter to topological phase conversion: fundamentals, materials, physical systems for phase conversions, and device applications. Mater Sci Eng R Rep 145:100620